RSC Advances

PAPER

View Article Online
View Journal | View Issue

Cite this: *RSC Adv.*, 2023, **13**, 4729

Crystal facet and Na-doping dual engineering ultrathin BiOCl nanosheets with efficient oxygen activation for enhanced photocatalytic performance†

Kunyu Chen,[a] Yiwei Huang,[a] Meina Huang,[c] Yanqiu Zhu,[ad] Ming Tang,[a] Renjie Bi[a] and Meiping Zhu *[ab]

Photocatalytic oxidation (PCO) based on semiconductors offers a sustainable and promising way for environmental remediation. However, the photocatalytic performance currently suffers from weak light-harvesting ability, rapid charge combination and a lack of accessible reactive sites. Ultrathin two-dimensional (2D) materials are ideal candidates to overcome these problems and become hotpots in the research fields. Herein, we demonstrate an ultrathin (<4 nm thick) Na-doped BiOCl nanosheets with {001} facets (Na-BOC-001) fabricated *via* a facile bottom-up approach. Because of the synergistic effect of highly exposed active facets and optimal Na doping on the electronic and crystal structure, the Na-BOC-001 showed an upshifted conduction band (CB) with stronger reduction potential for O_2 activation, more defective surface for enhanced O_2 adsorption, as well as the highest visible-light driven charge separation and transfer ability. Compared with the bulk counterparts (BOC-010 and BOC-001), the largest amount of active species and the best photocatalytic performance for the tetracycline hydrochloride (TC) degradation were achieved for the Na-BOC-001 under visible-light irradiation, even though it had slightly weaker visible-light absorption ability. Moreover, the effect of the Na doping and crystal facet on the possible pathways for TC degradation was investigated. This work offers a feasible and economic strategy for the construction of highly efficient ultrathin 2D materials.

Received 15th December 2022
Accepted 30th January 2023

DOI: 10.1039/d2ra08003f

rsc.li/rsc-advances

1. Introduction

Antibiotic contaminated wastewater has become a major worldwide crisis since it is hostile to human health and causes ecological imbalance. Photocatalytic oxidation (PCO) technology based on semiconductors driven by renewable solar energy has been regarded as one of the most promising strategies for alleviating the antibiotic pollution.[1,2] The photocatalytic activity of semiconductors under ambient conditions is highly dependent on the reactive oxygen species (ROS, *e.g.* $^{\bullet}O_2^-$ and $^{\bullet}OH$) with strong redox ability.[3] The generation of ROS is mainly subject to the charge separation and the molecular oxygen (O_2) activation over photocatalysts under light irradiation. Although remarkable progress has been made, the common semiconductors (*e.g.* TiO_2, ZnO, CdS and g-C_3N_4) still suffer from some bottlenecks such as insufficient visible light absorption and rapid recombination of photo-induced charges.[4–8] The visible light (380–780 nm) accounts for more than half of the full solar spectrum. Developing novel semiconductor based photocatalysts with enhanced visible-light-driven activation of O_2 is essential.

A new class of Aurivillius phase materials named bismuth oxyhalides (BiOX; X = Cl, Br and I) has attracted great interests in the fields of photocatalysis, such as hydrogen production, CO_2 reduction and pollutant degradation.[8–10] The BiOX has a sandwich substructure of $[X]^-$–$[Bi_2O_2]^{2+}$–$[X]^-$ with internal electric field (IEF) between layers, which is beneficial for promoting the charge separation and transfer along [001] direction.[11–13] The selectively exposed facets have significant influence on the electronic structure and surface properties of BiOX, thus strongly affecting the photoactivity. For example, Zhang's group have previously demonstrated that the single-crystalline BiOCl with exposed {001} facets (BOC-001)

[a]*State Key Laboratory of Featured Metal Materials and Life-cycle Safety for Composite Structures, School of Resources, Environment and Materials, Guangxi University, Nanning 530004, P. R. China. E-mail: meipingzhu@gxu.edu.cn*

[b]*Guangxi Key Laboratory of Petrochemical Resource Processing and Process Intensification Technology, Guangxi University, Nanning 530004, P. R. China*

[c]*College of Materials and New Energy, South China Normal University, Shanwei 516625, P. R. China*

[d]*College of Engineering, Mathematics and Physical Sciences, University of Exeter, Exeter, EX4 4QF, UK*

† Electronic supplementary information (ESI) available. See DOI: https://doi.org/10.1039/d2ra08003f

displayed superior photodegradation activity to and more efficient photoinduced charge separation than those with {010} facets (BOC-010) under UV light, which was ascribed to the favorable IEF.[14] They also reported that the activation of O_2 into $^{\bullet}O_2^-$ over the BOC-001 under UV light irradiation was more efficient in comparison to the BOC-010.[15] In addition, the positive contribution of (001) crystal surface exposure in the photocatalytic performance has been also reported by Zhou *et al.* They found that BiOCl with (001) crystal facets and carbon quantum dot decoration could achieve the highest TC removal efficiency (up to 98%) even under visible light irradiation.[16] In this regard, facet engineering provides a potential pathway for designing highly efficient BiOX based photocatalysts.

Among the BiOX family, BiOCl has attracted increasing attention for its advantages such as suitable band edge, low toxicity and earth abundance.[17] However, the photocatalytic performance of BiOCl under visible light irradiation is restricted by its weak O_2 activation ability. Up to now, surface defect particularly oxygen vacancies (OVs) engineering has been widely explored to improve the visible-light-driven O_2 activation and the ROS generation in BiOCl and other Aurivillius phase materials such as $(BiO)_2OHCl$ and Bi_2MoO_6.[18,19] Various strategies have emerged for the construction of surface defects, such as nonmetal or metal doping, solvothermal reduction and liquid-exfoliation, of which, the nonmetal or metal doping has been proved as one of the most facile and effective strategies. For example, Deng *et al.* prepared $BiOCl_xBr_{1-x}$ and $BiOCl_xI_{1-x}$ solid solutions by *in situ* doping of nonmetal ions (Br^- and I^-) during the synthesis of BiOCl. Both $BiOCl_{0.3}Br_{0.7}$ and $BiOCl_{0.7}I_{0.3}$ showed 97.7% and 100% of Cr(VI) removal rate under visible light irradiation, respectively, which were attributed to the doping-induced OVs that not only broadened the light absorption range, but also improved the charge separation efficiency.[20] Very recently, Huang and co-workers reported a strontium (Sr) doping strategy for fabricating BiOI with OVs, resulting in almost 10 times of degradation activity higher than pristine BiOI under visible light. Sr is an alkaline earth metal featured with nontoxicity and low cost, especially trapping electron effect which play a vital role in the OVs generation and charge separation. Similarly, alkaline metals, *e.g.* Na and K, are also beneficial for promoting the OVs creation and charge separation under visible light irradiation, which has been realized on different type of semiconductors such as g-C_3N_4 and $ZnWO_4$.[21–23] However, the investigation of effects of alkaline metal doping on the visible-light-driven catalytic properties of BiOCl remains scarce.

In comparison to the reported bulk BiOCl, a higher ratio of unsaturated coordination atoms in the ultrathin BiOX is more beneficial for promoting the formation of the surface defects, which can further boost the charge separation and O_2 activation, in addition to the enhanced adsorption for target pollutant molecules.[24,25] Xie's group[26] firstly reported that as the thickness of BiOCl with highly active {001} facets decreased from 30 nm to 2.7 nm, the photo-degradation activity was significantly improved with the enhanced adsorption performance, increased charge separation efficiency and more favorable band edges for O_2 activation. Wang *et al.*[9] prepared the hierarchical BiOBr microflower consisting of ultrathin nanoflakes with highly exposed {001} facets. They found that the ultrathin microstructure with exposed {001} facets is favorable for promoting the generation of surface OVs and boosting the charge separation/transfer, resulting in the high photodegradation performance for *ortho*-dichlorobenzene under visible light irradiation. Therefore, the synthesis of ultrathin BiOX nanosheets with highly exposed {001} facets is desirable and critical for achieving abundant adsorption sites and highly efficient photocatalytic performance. Liquid-phase exfoliation and surfactant self-assembly are two common and effective strategies for the synthesis of ultrathin BiOCl nanosheets. However, the low production yield, time-consuming procedures involving with unsafe use of organic solvents, and residues of inert surfactants severally restricted their large-scale practical applications.[27,28] Hence, it is imperative and challenging to develop a scalable, green and controllable technique for fabricating ultrathin BiOCl nanosheets with highly exposed {001} facets.

Herein, ultrathin Na-doped BiOCl nanosheets with exposed {001} facets (Na-BOC-001) have been fabricated *via* a facile one-step facet regulation and Na doping. The synergistic effects of crystal facet engineering and Na doping on the structural and electronic changes will be studied and discussed in detail. The performance of photocatalytic degradation for TC under visible light irradiation will be evaluated. Finally, the possible mechanism for the TC photo-degradation process will be analyzed. This work will provide a guidance on designing of efficient, ultrathin, semiconductor based photocatalysts with high performance.

2. Experimental section

2.1. Chemicals

Bismuth nitrate penta-hydrate ($Bi(NO_3)_3\cdot 5H_2O$), sodium dodecylbenzene sulfonate ($C_{18}H_{29}NaO_3S$), and sodium hydroxide (NaOH) were purchased from Aladdin Biochemical Technology Co., Ltd. Hydrochloric acid (HCl), ammonium hydroxide ($NH_3\cdot H_2O$) and nitric acid (HNO_3) were purchased from Sinopharm Chemical Reagent Co., Ltd. All chemicals used in this study were analytical grade without further purification. Deionized water was used for all the experiments.

2.2. Synthesis of photocatalysts

2.2.1. BiOCl with {010} and {001} exposed facets (BOC-010 and BOC-001). Typically, 10 mmol of $Bi(NO_3)_3\cdot 5H_2O$ was firstly dissolved in 60 mL of HCl aqueous solution (2 M) to form a transparent solution under continuous stirring. Then, 6 mmol of surfactant ($C_{18}H_{29}NaO_3S$) was added into the above solution and stirred for 30 min. The pH of the mixtures was adjusted to a certain value (0.6 or 5) using HNO_3 (2 M) and $NH_3\cdot H_2O$ (2 M) aqueous solution. After 30 min of stirring under ambient condition, the resultant precipitate was collected by filtration and washed with absolute ethanol and water thoroughly. The samples were finally obtained after dried at 60 °C overnight,

which were denoted as BOC-010 and BOC-001, corresponding to pH value of 0.6 and 5, respectively.

2.2.2. Na-doped BiOCl with {010} and {001} exposed facets (Na-BOC-010 and Na-BOC-001). Samples (Na-BOC-010 and Na-BOC-001) were separately fabricated under the similar conditions as BOC-010 and BOC-001, besides the addition of 20 mL of NaOH aqueous solution as the Na^+ source. The resulting samples with 0.15, 0.35, 0.50 and 0.60 mM of Na^+ (relative to the 80 mL of precursor solution in total) addition were labeled as *x*-Na-BOC-001 (x = 0.15, 0.35, 0.50 and 0.60, respectively). The sample with the highest degradation efficiency under visible light irradiation was selected as the representative of *x*-Na-BOC-001 and renamed as Na-BOC-001. By comparison, the added Na^+ concentration ([Na^+]) for Na-BOC-010 was consistent with that of the Na-BOC-001.

A schematic synthesis procedure of BOC-010, BOC-001 and Na-BOC-001 is shown in the following Scheme 1.

2.3. Characterization

Scanning electron microscope (SEM, Sigma 300, Zeiss Gruppe) and energy-dispersive X-ray spectroscopy (EDS) were employed to investigate the morphology and elemental distribution, respectively. More microstructural information was obtained by transmission electron microscope (TEM, FEI-Tecnai G2F20) and high-resolution transmission electron microscope (HRTEM, JEOL-JEM 2100 F) with an accelerating voltage of 200 kV. Atomic force microscopy (AFM, HITACHI 5100N) was used to study the thickness of samples. The structure and crystallinity of the as-prepared samples were analyzed by power X-ray diffractometer (XRD) (A24A10, Bruker) with a Cu Kα as the radiation source under 40 kV and 30 mA. The laser Raman spectrometer (Renishaw 1500S) was utilized for the Raman spectra with a laser (532 nm) as the excitation source. Surface elemental compositions and chemical states were analyzed by X-ray photoelectron spectrometer (XPS, Thermo ESCALAB 250XI+) with an Al Kα X-ray radiation source ($h\nu$ = 1486.6 eV). The valence band (VB) position was examined by the VB-XPS analysis using another XPS spectrometer (Thermo Fisher Scientific K-Alpha).

The Branauer–Emmett–Teller (BET) specific surface area was evaluated on a N_2 isothermal adsorption/desorption apparatus (Micromeritics, USA) at 77 K. EPR and ESR spectra were acquired by an electron paramagnetic resonance spectrometer (Bucker A300) at 298.15 K under darkness and visible light irradiation (λ > 420 nm). O_2-temperature programmed desorption (O_2-TPD) profiles were obtained by an automatic chemisorption analyzer (Micromeritics AUTOCHEM II 2920). Prior to the O_2-TPD test, 100 mg of sample was firstly pretreated in a He flow (50 mL min^{-1}) at 300 °C for 1 h, then cooled to 50 °C. During the test, the sample was purged with O_2/He (5 vol%, 50 mL min^{-1}) flow at 50 °C for 1 h, and then swept by He flow (50 mL min^{-1}) in 50–300 °C with a heating rate of 10 °C min^{-1} and the desorbed gas was detected.

UV-Vis diffuse reflection spectra (UV-Vis DRS) were recorded using a UV-Vis spectrophotometer (UV-3600Plus, SHIMADZU) for investigating the optical absorption property. The bandgap energy (E_g) value can be estimated according to the Kubelka–Munk formula (eqn (1)):

$$ahv = A(hv - E_g)^{n/2} \quad (1)$$

where a, h, v, A are absorption coefficient, Planck's constant, light frequency, and proportionality constant, respectively. The value of n is 4 since BiOCl is an indirect bandgap semiconductor.[29] In detail, E_g can be estimated from plotting $(\alpha hv)^{1/2}$ *vs.* hv following the Tauc approach based on the obtained UV-Vis DRS data.

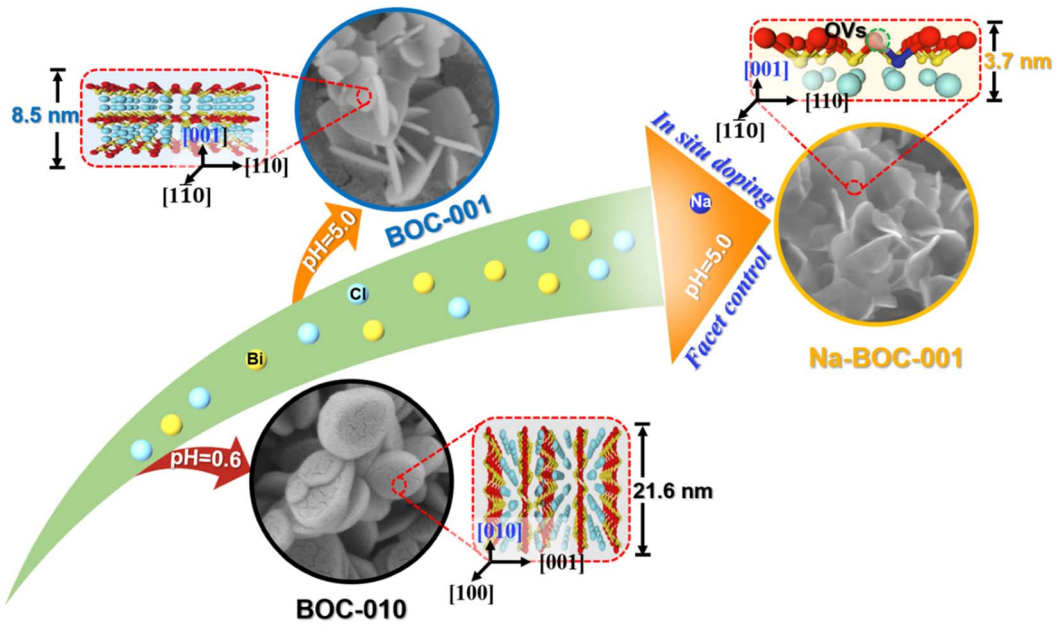

Scheme 1 Schematic synthesis procedure of BOC-010, BOC-001 and Na-BOC-001.

Photoluminescence (PL) spectra were recorded using a steady state and transient fluorescence spectrophotometer (OmniFluo990LSP, Zolix) with an excitation wavelength of 300 nm. Photocurrent response profiles, electrochemical impedance spectroscopy (EIS-Nyquist) plots and Mott–Schottky plots were measured by an electrochemical workstation (CHI660E) in a three-electrode system. Typically, the FTO glass coated with samples, Ag/AgCl and platinum wire were used as the working, reference and counter electrodes, respectively. Besides, the Na_2SO_4 solution was used as the electrolyte (pH = 5.3). During the photocurrent response and electrochemical impedance spectroscopy (EIS) test, the working electrode was irradiated by a 300 W xenon lamp (CEL-HXF300-T3, Beijing China Education Au-light Co., Ltd) with a UV cut-off filter (visible light, $\lambda > 420$ nm). For the preparation of the working electrode, a certain amount of sample was dispersed in 95 μL of ethanol to form a homogeneous solution (100 mg mL^{-1}). Then, 5 μL of Nafion solution was added into the above mixture solution under ultrasonication. Finally, the working electrode was obtained after coating of the above colloidal solution on a slice of clean FTO glass (1 × 2 cm^2) and vacuum drying for ~6 h.

2.4. Photocatalytic activity and intermediates analysis

Photocatalytic activity of the as-prepared samples was evaluated by the removal of TC. A 250 mL of open cylinder quartz glass container and a 300 W xenon lamp (CEL-HXF300-T3, Beijing China Education Au-light Co., Ltd) with a 420 nm cut-off filter were employed as the reactor and light source, respectively. The light intensity is 220, 251 and 700 mW cm^{-2} for visible, UV and UV-visible light, respectively, which were monitored at a distance of 15 cm from the light source to the center of the photocatalytic reactor and recorded by using an optical power meter (CEL-NP2000-10A, Beijing China Education Au-light Co., Ltd). For each photocatalytic test, 50 mg of sample was dispersed to 100 mL of TC aqueous solution (20 mg L^{-1}) under continuous stirring (~500 rpm). Prior to the irradiation, the above suspension was magnetically stirred under darkness for 30 min to reach adsorption–desorption equilibrium for the TC. Subsequently, 3 mL of liquid sample was extracted from the reaction suspension at certain intervals and collected through a syringe filter (0.45 μm, polyethersulfone ultrafiltration membrane) to remove the catalyst particles. The filtrates were analyzed at the absorption wavelength of 357 nm by a UV-Vis spectrophotometer (TU-1900, PerkinElmer). The degradation efficiency (η) of TC was calculated by eqn (2) as follows:

$$\eta = \left(1 - \frac{C_t}{C_0}\right) \times 100\% \quad (2)$$

where C_0 and C_t (mg L^{-1}) represent the concentrations of TC at initial and certain irradiation time, respectively.

To quantitatively elucidate the reaction kinetics for TC degradation, the following pseudo first-order model (eqn (3)) was utilized for the analysis of the experimental data:

$$-\ln\left(\frac{C_t}{C_0}\right) = kt \quad (3)$$

where k is a constant of pseudo first-order rate; t (min) is the reaction time.

Organic carbon mineralization of TC solution during photocatalysis was investigated by total organic carbon (TOC) analysis using a TOC analyzer (Shimadzu TOC-L CPH). The intermediate products were determined by a low-resolution mass spectrometry (MS) equipped with an electrospray interface (ESI) as the ion source, and the fragment scanning mode is negative ion mode with the m/z range of 64–500.

3. Results and discussion

3.1. Morphology, thickness and elemental distribution

The morphology and microstructure of the as-prepared BOC-010, BOC-001 and Na-BOC-001 samples were investigated by using SEM and TEM. As shown in Fig. 1a, the BOC-010 exhibits a circular pie shaped morphology with lateral lengths varying from 200 to 300 nm. In Fig. 1b, it can be observed that BOC-001 is composed of 2D nanoplates with higher standing-up ratio and smaller thickness than the BOC-010, which demonstrates that the crystal planes and thickness of BOC can be regulable by adjusting the pH during the BOC growth. Noteworthy, semi-transparent nanosheets without compromising the high ratio of standing-up planes are obviously visible after the Na doping (Fig. 1c).

The crystal microstructure of the as-prepared samples was further studied using the high-resolution TEM (HRTEM). As shown in Fig. 1d, the Na-BOC-001 exhibits two distinct lattice fringes with interplanar crystal spacings of 0.194 nm and 0.275 nm, which are ascribed to the (200) and (110) atomic planes of the lamellar Na-BOC-001, respectively. In addition, the corresponding fast Fourier transform (FFT) patterns display spot patterns with an angle of 45°, which is consistent with the theoretical angle between the (200) and (110) planes. This result reveals that the set of diffraction spots can be indexed to the [001] zone axis. According to the symmetry of tetragonal BiOCl, it can be deduced that the dominant exposed planes of Na-BOC-001 are {001} facets.[9,14] The BOC-010 with dominant facets of {010} and BOC-001 with dominant facets of {001} can be supported by Fig. S1.†

The AFM images and corresponding height profiles describe the thickness of Na-BOC-001 nanosheets, as shown in Fig. 1e. The Na-BOC-001 shows 3.65 nm of thickness, verifying the ultrathin nanosheets of Na-BOC-001 have been successfully fabricated by the facile Na doping and facet regulation strategy. To investigate the Na doping efficiency, SEM/EDS analyses of BOC-010, BOC-001 and x-Na-BOC-001 (x = 0.15, 0.35, 0.50 and 0.60) were applied and their results are shown in Fig. S2, S3† and 1g, respectively. The relative content of Na, Bi, O and Cl was summarized in Table S1.† The EDS images (Fig. S2 and S3†) display a uniform distribution of the Bi, O and Cl element in all samples. Additional Na element appears evenly in all of the x-Na-BOC-001 samples. As seen in Fig. S4 and Table S1,† the actual doping ratio of Na to Bi in x-Na-BOC-001 (x = 0.15, 0.35, 0.50 and 0.60) is 1.30, 2.63, 5.83 and 5.10%, respectively, according to the SEM/EDS analyses. The morphology and thickness of x-Na-BOC-001 (x = 0.15, 0.35, 0.50 and 0.60) were

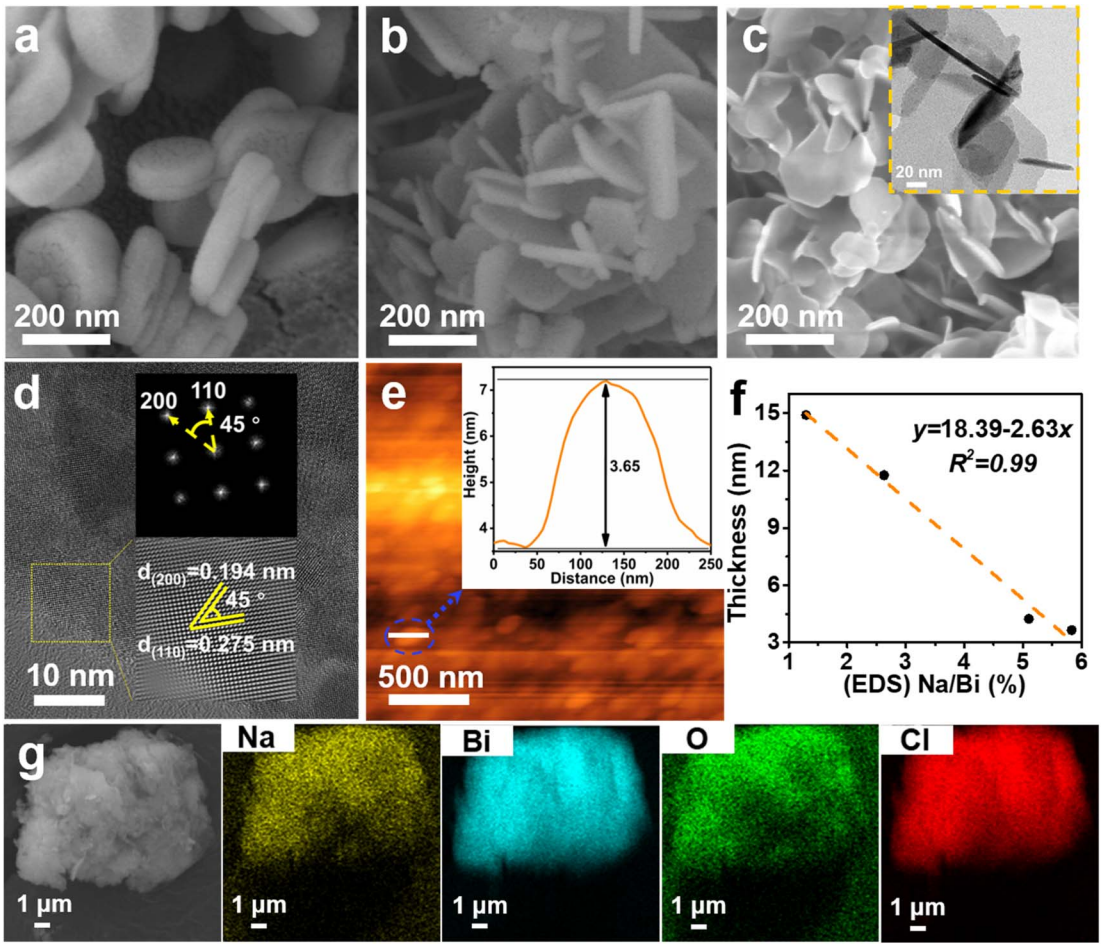

Fig. 1 SEM images of (a) BOC-010 and (b) BOC-001. (c) SEM image and TEM image (inset), (d) HRTEM image with enlarged view (lower inset) and SAED pattern (upper inset), (e) AFM image and corresponding height profile (inset), (f) thickness as a function of (EDS) Na/Bi (the dotted line shows the super-linear trend of thickness on the (EDS) Na/Bi), and (g) SEM image and corresponding EDS elemental mapping of Na-BOC-001.

further investigated by SEM and AFM, as displayed in Fig. S5 and S6,† respectively. As the added [Na^+] increased from 0.15 to 0.60 mM, the *x*-Na-BOC-001 samples show a morphology change from circular pie to ultrathin nanosheet (Fig. S5†). The exact thickness of *x*-Na-BOC-001 (x = 0.15, 0.35, 0.50 and 0.60) in Fig. S6† was measured as 14.91, 11.76, 3.65 and 4.24 nm, respectively. Interestingly, the thickness of *x*-Na-BOC-001 reduced with the increasing Na/Bi ratio (from EDS) (Fig. 1f). The result confirms the negative super-linear correlation between the thickness and the actual Na-doped ratio in the Na-BOC-001 samples. In addition, the other counterparts (0.50-Na-BOC-010, BOC-010 and BOC-001) show thicknesses of 24.4, 21.6 and 8.46 nm, respectively, as shown in Fig. S6.† Based on the above results, it can be concluded that the ultrathin Na-BOC-001 nanosheets with atomic layer thickness (<4 nm) and highly exposed {001} facets have been successfully prepared *via* simply adjusting the pH value of the precursor solution and controlling the [Na^+] during growth, and that the atomic layer thickness of ultrathin Na-BOC-001 is attributed to the synergistic effect of {001} facets and Na doping.

3.2. Crystal structure

The crystal phase and structure of the as-synthesized BOC-010, BOC-001 and Na-BOC-001 samples were identified by XRD. The results (Fig. 2a) display that all diffraction peaks of the samples match well with those of tetragonal BiOCl (JCPDS: 06-0249),[30] indicating the successful synthesis of the samples with highly pure phase. It is notable that the peaks ascribed to (001) plane of BOC-010 are much stronger than that of BOC-001. In addition, the BOC-010 show a clearly decreased intensity ratio of (110)/(001) peaks in comparison to that of BOC-001. These are attributing to that the crystal growth of BiOCl along *c* axis of BOC-010 was inhibited in the acidic growth condition (pH = 0.6),[31] which is in good agreement with the HRTEM results. Moreover, as seen in Fig. 2b, the Na-BOC-001 shows a slight shift to higher diffraction angle for the (110) peak compared with BOC-001, indicating the shrinkage of lattice according to Bragg equation. This result is ascribed to the Na doping effect and the resulted defects based on the charge compensation.

The effect of initial added [Na^+] on the structural change of Na-BOC-001 is shown in Fig. 2c. Compared with 0.15-Na-BOC-001, an obvious upshift is observed at the (110) peak position

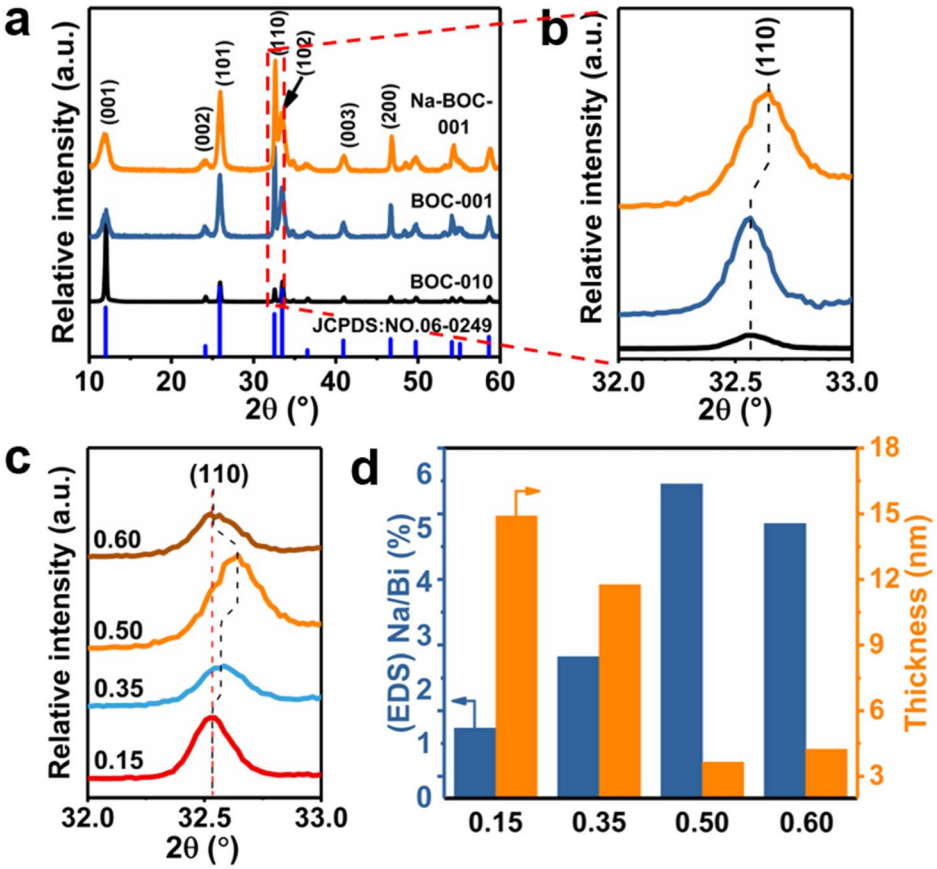

Fig. 2 (a) XRD patterns of the as-synthesized BOC-010, BOC-001 and Na-BOC-001 samples, (b) enlarged view of the marked area in (a). (c) Enlarged view of (110) diffraction peak in XRD patterns, and (d) (EDS) Na/Bi and thickness of *x*-Na-BOC-001 (x = 0.15, 0.35, 0.50 and 0.60) samples.

of 0.35-Na-BOC-001, which indicates the mild lattice shrinkage due to the increasing [Na^+]. As the [Na^+] further increased, the peak of 0.50-Na-BOC-001 shifts to the highest angle, demonstrating that the severe lattice shrinkage was presented at 0.50 mM of [Na^+].[32] However, 0.60-Na-BOC-001 exhibits an abnormally downshift back to the angle similar to 0.15-Na-BOC-001. A similar anomalous trend was observed from the doping efficiency of Na^+, that is, the actual doping ratio of Na/Bi in the samples reversely decreased as the [Na^+] increased from 0.50 to 0.60 mM (Fig. 2d). This can be attributed to the fact that the dominant doping sites of Na^+ was converted from the substitutional site to the interstitial site.[33] Generally, the interstitially doped Na ions have higher energy and less stability than the substitutional doped Na^+, which was accompany with the lattice expansion (as verified by the XRD results) and readily diffused to the surface and then lost after washing, leading to the reduction of the doping efficiency.[33,34] Interestingly, there is a positive correlation between the degree of lattice shrinkage and nanosheet thickness induced by the [Na^+] ranged from 0.15–0.50 mM. Hence, it can be concluded that the severe lattice shrinkage of Na-BOC-001 is mainly originated from the Na doping effect, which results in the ultrathin thickness.

The laser (λ = 532 nm) was utilized for the Raman spectra to confirm the vibrational normal modes of the samples (Fig. 3). The A_{1g}, B_{1g} and E_g denote the three center vibration modes for BiOCl due to the tetragonal structure (space group *P*4/*nmm*).[35] All samples exhibit two resembling peaks (143.6 and 199.4 cm^{-1}) and one weak peak at around 398 cm^{-1}. The peak at 143.6 and 199.4 cm^{-1} ascribed to the A_{1g} and E_{1g} internal Bi–Cl stretching mode, while the peak at around 398 cm^{-1} due to the E_g and B_{1g} modes caused by the vibration of oxygen atoms.[36] Compared with BOC-001, the Na-BOC-001 exhibits a blue shift from 143.6 to 144.7 cm^{-1}, while the Na-BOC-010 shifted from 200.7 to 199.4 cm^{-1} (red shift). These results indicated the crucial role of exposed facet and Na-doping dual engineering. In addition, the peak of all samples at around 399 cm^{-1} disappears due to the weak surface oxygen vibrations.[37]

The FTIR spectra were further employed to confirm the stretching mode of the samples (Fig. S7†). All samples appear the characteristic peaks of BiOCl, located at about 527 cm^{-1} and 1397 cm^{-1} were assigned to the Bi–O and Bi–Cl stretching mode, respectively.[29,38] The other peaks located at 1634 cm^{-1} and 3433 cm^{-1} can be indexed to the surface hydroxyl group and the chemisorbed H_2O.[39,40] From Fig. S7,† the Bi–O peak intensity of Na-BOC-001 was much weaker than BOC-001, and the peak shifted to higher wavenumber, which may be attributed to the substitution of Bi by Na ions. Similar results have also been observed in BOC-010 and Na-BOC-010.

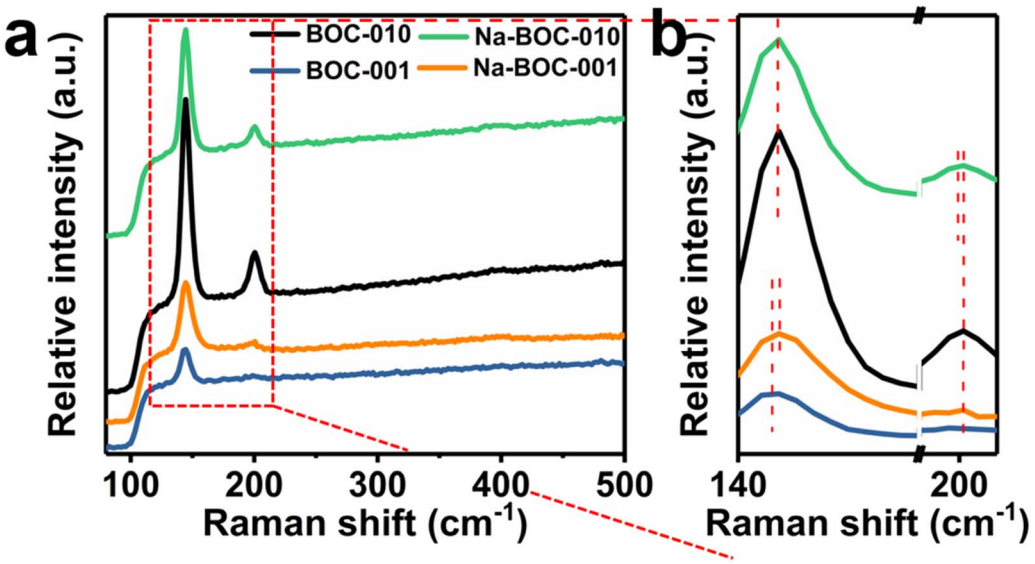

Fig. 3 (a) Raman spectra of Na-BOC-010, BOC-010, Na-BOC-001 and BOC-001 samples, (b) enlarged view of the marked area in (a).

3.3. Surface chemical states

XPS spectra were acquired to further study the surface elemental compositions and chemical states of the BOC-010, BOC-001 and Na-BOC-001 samples. The survey XPS spectra show that all samples are composed of Bi, O and Cl elements (Fig. S8†). Notably, an additional peak ascribed to Na 1s can be observed in the Na-BOC-001. The peak at 284.6 eV of C 1s was employed as calibration standard for other binding energies. The high-resolution Na 1s spectrum (Fig. 4a) exhibits a peak corresponding to the Na species centered at 1070.2 eV, reconfirming that the Na^+ has been successfully introduced into the Na-BOC-001,[21,41] which is in agreement with the EDS elemental mapping.

In the high-resolution Bi 4f spectra (Fig. 4b), two strong peaks assigned to Bi $4f_{7/2}$ and Bi $4f_{5/2}$ are presented in the BOC-010, BOC-001 and Na-BOC-001 samples. The splitting value between Bi $4f_{7/2}$ and Bi $4f_{5/2}$ of all samples is ~5.3 eV.[42] The Bi 4f peaks of Na-BOC-001 slightly shift toward a lower binding energy than those of BOC-010 and BOC-001. In Fig. 3c, the Cl 2p spectra of the samples can be fitted with two peaks corresponding to Cl $2p_{3/2}$ and Cl $2p_{1/2}$, respectively. Similar to the Bi 4f peaks, a negative shift is observed in the binding energy of Cl 2p peaks for Na-BOC-001 compared with the BOC-010 and BOC-001, suggesting that the electron-withdrawing of Cl and Bi originates from the interfacial electron interaction between Na and Na-BOC-001.

The high-resolution O 1s XPS spectra (Fig. 4d) of the samples are fitted into three peaks (O_α, O_β and O_ε), which can be indexed to lattice oxygen, chemically and physically adsorbed oxygen species (*e.g.* O_2, –OH) over oxygen vacancies (OVs), respectively.[38,43] Na-BOC-001 presents a lower binding energy shift for the O_ε peak in comparison with BOC-010 and BOC-001, which demonstrates that the electron redistribution around O atom in Na-BOC-001 is owing to the Na doping effect. The relative content of the O 1s splitting peaks (O_α, O_β and O_ε) is summarized in Table S2.† Compared with BOC-010 and BOC-001, Na-BOC-001 exhibits a dramatically increased proportion (22.1%) of O_ε for the physically adsorbed oxygen species whereas a decreased ratio (7.0%) of the O_β. The result indicates a preferential adsorption of the weaker bonding oxygen species on the surface of Na-BOC-001 owing to the Na doping effect.

3.4. Oxygen vacancies and oxygen adsorption

The solid-state EPR analysis was applied to further probe the surface defect of the samples (BOC-010, BOC-001 and Na-BOC-001). As displayed in Fig. 5a, an obvious peak centered at the *g*-factor value of 2.003 is presented in the EPR spectra of all samples under darkness and visible light irradiation, which is ascribed to the defect of surface OVs.[30] In the dark, BOC-010 and BOC-001 show almost similar intensities for the EPR peak, whereas slightly higher intensity for the Na-BOC-001 than that of BOC-001 and BOC-010, directly verifying the higher concentration of synthetically introduced surface OVs on Na-BOC-001. This result is in good agreement with the XPS result. Moreover, under visible light irradiation for 20 min, the concentration of surface OVs significantly increases over the samples. Among them, Na-BOC-001 presents the highest OVs content. These results indicate the Na doping is beneficial for promoting the generation of light-controlled OVs on the surface of BiOCl. Compared with the synthetically introduced OVs which is unstable, the light-controlled OVs have high potential as sustainable active sites for their better reversibility in adsorption and desorption of oxygen species (*e.g.* O_2 and H_2O),[44] which is beneficial for promoting the O_2 activation.

To determine the adsorption interaction between oxygen species and the surface defects of the prepared samples, O_2-TPD assessment was conducted and the results are shown in Fig. 4b. No obvious TCD signal of oxygen species in the range of 50–

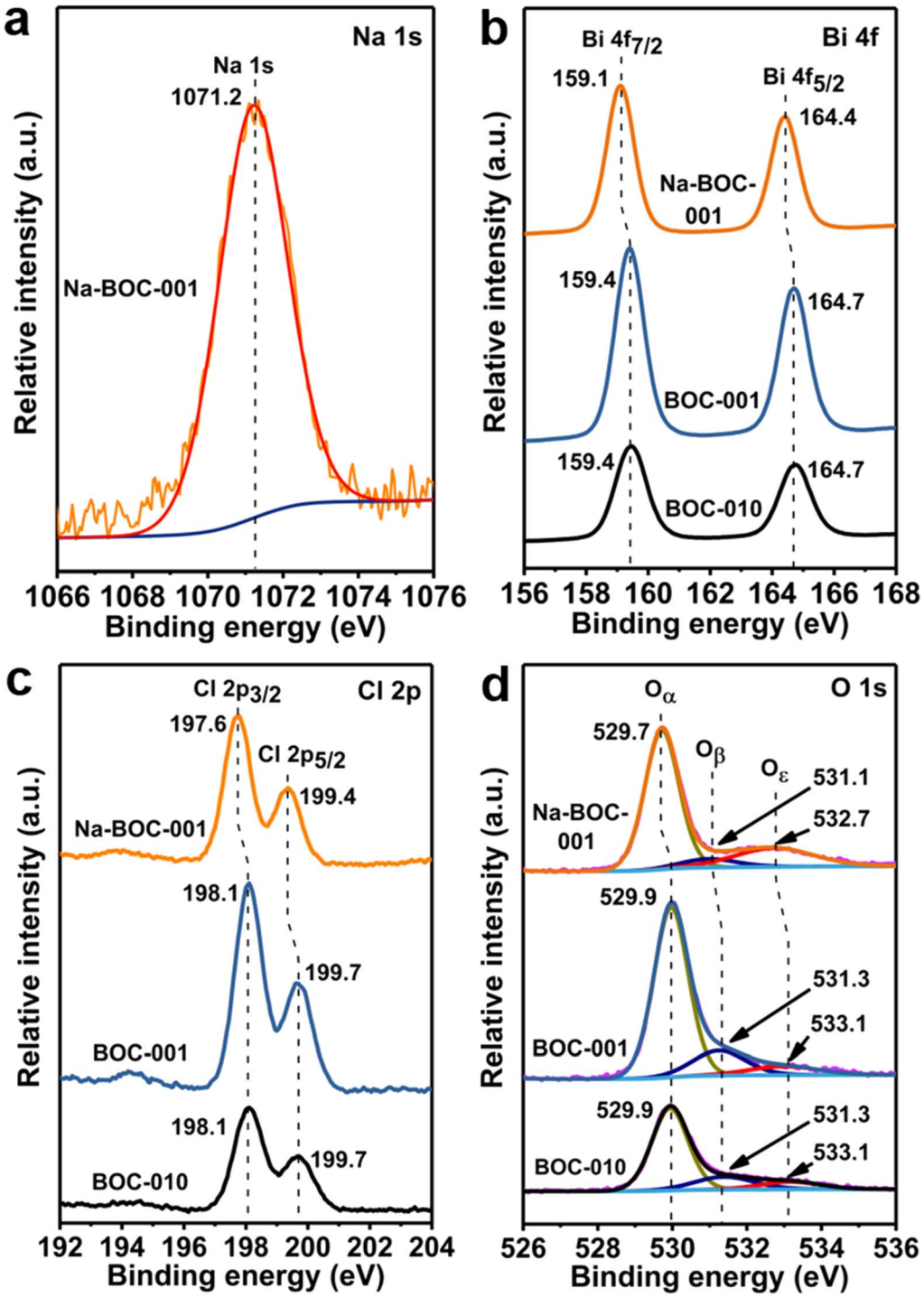

Fig. 4 High-resolution (a) Na 1s XPS spectrum of Na-BOC-001. High-resolution (b) Bi 4f, (c) Cl 2p and (d) O 1s XPS spectra of BOC-010, BOC-001 and Na-BOC-001 samples.

300 °C for BOC-010, BOC-001, by contrast, Na-BOC-001 displays a strong O_2 desorption peak centered at ~110 °C, which is ascribed to the physically adsorbed O_2. This might be associated with the enriched surface OVs and the large specific surface area of the ultrathin Na-BOC-001 (Fig. S9†). Hence, Na-BOC-001 is expected to display an improved performance in O_2 activation and ROS generation.[45]

3.5. Photoexcited charge separation

The PL spectra of the as-prepared samples were obtained at the excitation wavelength of 300 nm. As shown in Fig. 6a, all samples display similar PL band in range of 320–500 nm but different intensities, which have the following order: BOC-010 > BOC-001 > Na-BOC-010 > Na-BOC-001. It is noticeable that the

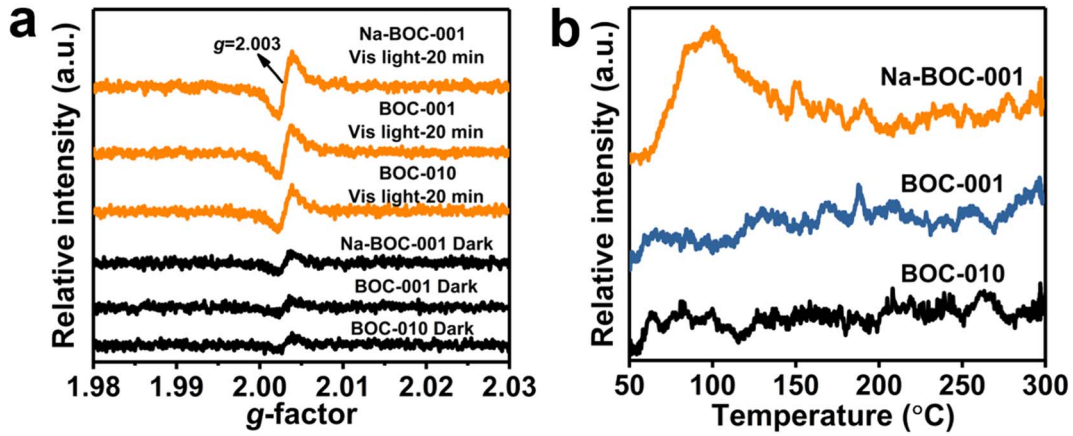

Fig. 5 (a) Solid-state EPR spectra under darkness and visible-light irradiation (λ > 420 nm) and (b) O_2-TPD profiles of BOC-010, BOC-001 and Na-BOC-001 samples.

Na-BOC-001 exhibited much lower PL intensity than the other three samples, which indicated that the lowest charge recombination rate was achieved over the Na-BOC-001.[46]

Photocurrent response profiles were obtained to evaluate the photoexcited charge separation of the BOC-010, BOC-001 and Na-BOC-001 samples driven by the solar light in the visible range (λ > 420 nm). As shown in Fig. 6b, all three electrodes coated with the as-prepared samples exhibit rapid and reproducible photocurrent responses along with the light on/off cycles. The photocurrent of Na-BOC-001 (0.21 μA cm^{-2}) is obviously higher than that of BOC-001 (0.17 μA cm^{-2}), Na-BOC-010 (0.19 μA cm^{-2}) and BOC-010 (0.10 μA cm^{-2}), showing the maximum efficiency of the photo-exited charge separation in the Na-BOC-001. It can be concluded that both the Na doping and the exposed {001} are conducive to the increase of photocurrent. The enhancement in Na-BOC-001 can be owing to the synergistic effect of Na doping and facet engineering. On one hand, the reduction in the number of atomic layers for Na-BOC-001 resulted from Na doping is beneficial for shortening the electron migration distance (as verified in AFM results). On the other hand, the Na dopant acted as interfacial electron transfer bridge to accelerate the charge separation, as reported.[41]

In addition, the EIS plots (Fig. 6c) were also used to evaluate the efficiency of charge separation and transfer over the samples.[47] A smaller semicircle radius corresponds to a lower charge-transfer resistance value of R_t, which reflects a higher charge separation and transfer efficiency.[48] In this regard, it is obvious that the order of charge separation efficiency for all samples derived from EIS is in good agreement with those of PL and I–t under similar irradiation condition. Notably, the Na-BOC-001 indeed has the fastest charge separation and migration rates.

3.6. Optical absorption and band structure

The UV-Vis DRS spectra were recorded to investigate the optical absorption performance of the BOC-010, BOC-001 and Na-BOC-001 samples. As shown in Fig. 7a, the Na-BOC-001 shows an obviously enhanced absorption in the UV region in comparison to BOC-010, BOC-001, which is mainly due to the interfacial electron interaction between the Na and Na-BOC-001. Although Na-BOC-001 and BOC-001 displayed similar absorption edge in the UV region (~360 nm), they showed urbach trails and obvious light absorption in the visible region. This implied the appearance of electronic states appeared between VB and CB,[49] which may be related to the electron cloud enriched around with the surface and bulk defects (*e.g.*, OVs) over the BiOCl samples.[50] The Na-BOC-001 exhibited stronger UV absorption

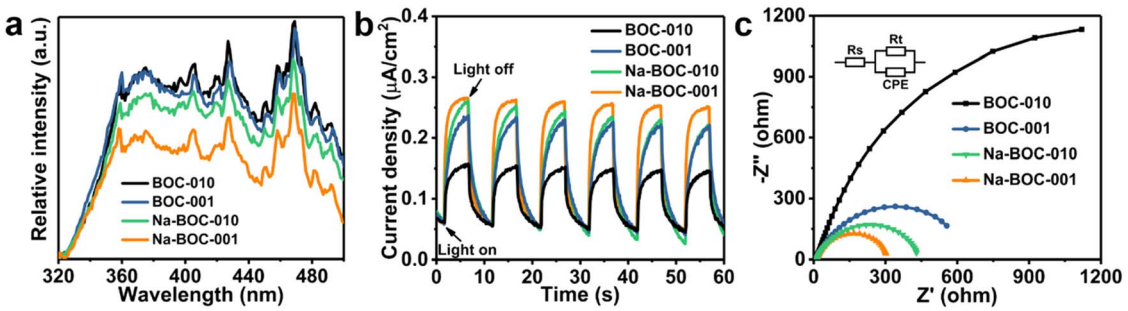

Fig. 6 (a) PL spectra of the as-prepared BOC-010, BOC-001, Na-BOC-010 and Na-BOC-001 samples with an excitation wavelength of 300 nm; (b) photocurrent response profiles and (c) EIS-Nyquist plots of the as-prepared BOC-010, BOC-001, Na-BOC-010 and Na-BOC-001 samples under visible-light illuminations (λ > 420 nm).

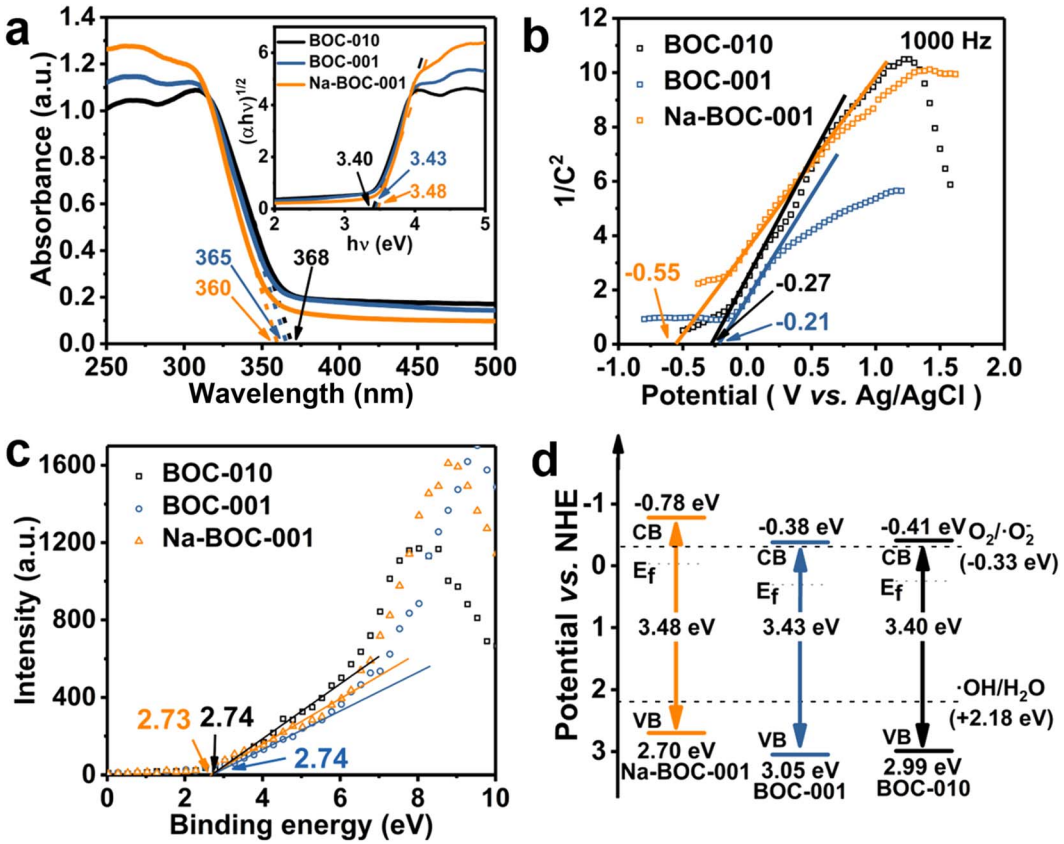

Fig. 7 (a) UV-Vis DRS spectra and the corresponding bandgap energies estimated from the plots of $(\alpha h\nu)^{1/2}$ *versus* $h\nu$ following the Tauc approach (inset), (b) VB-XPS spectra, (c) Mott–Schottky plots measured in 0.5 M Na_2SO_4 aqueous solution (pH = 5.3), (d) energy band diagram of BOC-010, BOC-001 and Na-BOC-001.

and slightly weaker visible absorption than that of BOC-001, which could be attributed to the Burstein–Moss effect associated with the cation-ion doping. According to the Tauc approach, the estimated E_g of BOC-010, BOC-001 and Na-BOC-001 are 3.40, 3.43 and 3.48 eV (Fig. 7b), respectively. The bandgap of Na-BOC-001 is broader than that of BOC-010 by 0.08 eV, which is attributed to the synergistic effect of the Na doping and facet engineering.

To further reveal the specific band edges of the BOC-010, BOC-001 and Na-BOC-001, VB-XPS and Mott–Schottky plots show the direct VB position, and their CB positions can be estimated by combining with the E_g value. As shown in Fig. 6c, the flat-band potentials (E_{fb}) of BOC-010, BOC-001 and Na-BOC-001 are estimated to be −0.27, −0.21 and −0.55 V (*vs.* Ag/AgCl), respectively. Generally, the Fermi level (E_f) equals to the flat-band potential (E_{fb}), since the BOC-010, BOC-001 and Na-BOC-001 are n-type semiconductors.[51] Furthermore, the E_{fb} (*vs.* Ag/AgCl) can be transformed into normal hydrogen electrode (NHE) level by the Nernst equation (eqn (3)):

$$E_{NHE} = E_{Ag/AgCl} + 0.05916pH + E^0_{Ag/AgCl}$$

Hence, the E_f of BOC-010, BOC-001 and Na-BOC-001 are 0.25, 0.31 and −0.03 V (*vs.* NHE), respectively. Besides, the energy gaps between E_f and VB of BOC-010, BOC-001 and Na-BOC-001 estimated from the VB-XPS results are 2.74, 2.74, 2.73 V, respectively. Therefore, the VB positions of BOC-010, BOC-001 and Na-BOC-001 are 2.99, 3.05, 2.70 V, respectively. According to the empirical formula (eqn (4)):

$$E_{VB} = E_{CB} + E_g \quad (4)$$

CB positions are calculated to be −0.41, −0.38, −0.78 V for BOC-010, BOC-001 and Na-BOC-001, respectively. Based on the deduction from the above calculations, the energy band diagram of BOC-010, BOC-001 and Na-BOC-001 can be plotted and is shown in Fig. 7d.[52] The BOC-010 and BOC-001 have the same CB potentials (−0.39 V), which are a little enough for oxygen activation and oxygen species generation ($O_2/{}^{\bullet}O_2^-$, −0.33 V). Particularly, Na-BOC-001 displays much more negative CB potential (−0.75 V) than the other two samples, which is favorable for the O_2 activation and attributed to the Na doping.

3.7. Reactive oxygen species

ESR spectra were used to analyze the ROS and the results are shown in Fig. S10, S11† and 8. It can be seen that there is no ${}^{\bullet}O_2^-$ and ${}^{\bullet}OH$ generated in the dark for the BOC-010, BOC-001, and Na-BOC-001 samples (Fig. S10 and S11†). The ROS signal could be detected when the visible light was irradiated for 3 min

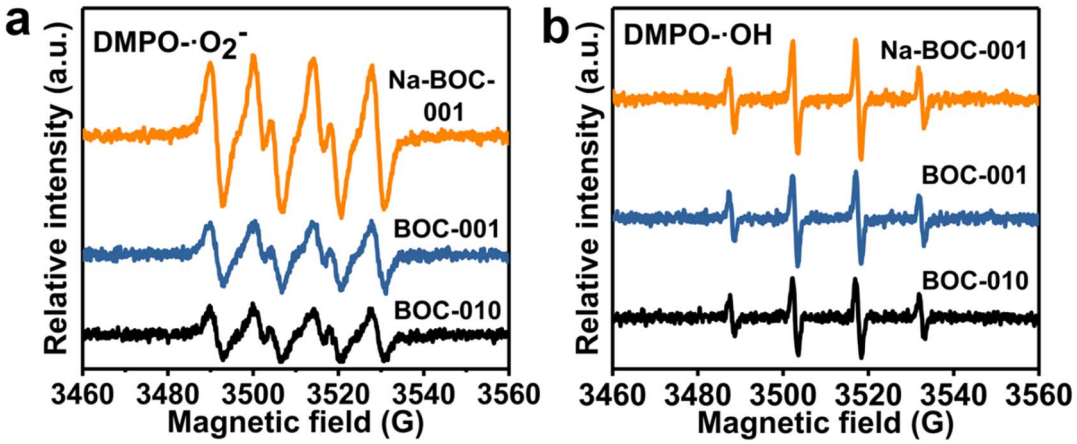

Fig. 8 ESR spectra of (a) DMPO–$^{\cdot}O_2^-$ and (b) DMPO–$^{\cdot}OH$ over BOC-010, BOC-001, and Na-BOC-001 under visible light irradiation for 3 min.

for all samples (Fig. 8). The difference in the $^{\cdot}O_2^-$ and $^{\cdot}OH$ signal intensities between the BOC-010 and BOC-001 is negligible. However, a significantly enhanced intensity of $^{\cdot}O_2^-$ is observed in the Na-BOC-001 compared with the BOC-010 and BOC-001, illustrating the highly efficient visible-light-driven O_2 activation of Na-BOC-001. This is mainly attributed to the defective surface with preferential adsorption of O_2 and efficient separation of photo-exited charges owing to the synergistic effect of Na doping and {001} facets.

Besides, the signal of $^{\cdot}OH$ species of Na-BOC-001 is also stronger than that of BOC-010 and BOC-001, even though more unfavorable VB potential of Na-BOC-001 for the direct generation of $^{\cdot}OH$ species (Fig. 7d).[53] According to the result, it is likely that more negative CB potential resulted from the Na doping are also vital for the efficient O_2 activation and ROS generation over Na-BOC-001 under visible light irradiation.

3.8. Photocatalytic activity

The photocatalytic activity of the samples was evaluated by the degradation of TC in air under visible light irradiation. The varied concentrations of TC in the degradation process were recorded by the UV-Vis absorption spectra and displayed in Fig. S12–S16.† The time–course curves of relative concentrations (C_t/C_0) are plotted in Fig. S16† and 9 based on the variation of TC absorbance centered at 357 nm. As displayed in Fig. S17,† all samples (BOC-010, Na-BOC-010, BOC-001 and Na-BOC-001) achieved the adsorption equilibrium within 30 min under darkness. It is notable that Na-BOC-001 exhibited the highest adsorption efficiency (~47%), which is 6.35, 6.63 and 2.33 times higher than that of BOC-010, Na-BOC-010 and BOC-001, respectively. This can be attributed to the increased specific surface area and enhanced oxyphilic surface of ultrathin Na-BOC-001 since the TC molecules is rich in oxygen-containing groups. However, the Na-BOC-010 displayed an inconspicuous change compared with BOC-010. These results indicate that it is the synergistic effect of Na doping and facet regulation that enhanced the TC adsorption capacity over BOCs.

The effect of $[Na^+]$ on the photocatalytic degradation of TC is presented in Fig. 9a. The removal efficiency over the *x*-Na-BOC-001 ($x = 0.15$, 0.35, 0.50 and 0.60) increased with the increases of reaction time. Interestingly, as shown in Fig. 9b, there is a positive dependence between the maximum removal efficiency and the (EDS) Na/Bi ratio with the addition of $[Na^+]$ ranged from 0.15–0.50 mM, which exhibits a negative correlation with the thickness (Fig. 1f). Among them, the 0.50-Na-BOC-001 displays the highest removal efficiency, hence it was selected as the representative of *x*-Na-BOC-001 series samples and renamed as Na-BOC-001 in the following discussion. To evaluate the synergistic effect of Na doping and facet engineering on the photocatalytic activity of BOCs, the removal efficiency towards TC under visible light irradiation over BOC-010, Na-BOC-010, BOC-001 and Na-BOC-001 was investigated and shown in Fig. 9c. The TC removal over BOC-010, Na-BOC-010, BOC-001 and Na-BOC-001 samples reached an equilibrium within an irradiation time of ~60 min, and their maximum removal efficiency was calculated to be 27, 44, 75 and 87%, respectively. It is noted that both Na-doped samples (Na-BOC-010 and Na-BOC-001) displayed much higher photocatalytic efficiencies than their corresponding undoped samples (BOC-010 and BOC-001), indicating the positive role of Na doping in promoting the photocatalysis of TC over BOCs. Moreover, the apparent rate constant of BOC-010, BOC-001, Na-BOC-010 and Na-BOC-001 is estimated to be 0.00708, 0.02534, 0.01005 and 0.03095 min^{-1}, respectively, as seen in Fig. S18 and Table S5.† Obviously, Na-BOC-001 also displayed the highest kinetic rate in the degradation process. The removal rate of TC under irradiation without catalyst is negligible (Fig. 9c and S12†), which indicated that the TC is much stable and resistant to the photodegradation caused solely by the light. These results demonstrate that superb photocatalytic activity for TC removal was achieved for the Na-BOC-001, which are mainly attributed to the increased photoexcited charge separation efficiency and enhanced visible-light-driven O_2 activation owing to the synergistic effect of Na doping and {001} facets. In particular, this effect has resulted in a significant enhancement of the intensity of OVs in all BOC samples after 20 min of visible light irradiation, which was more pronounced in Na-BOC-001, as shown in the above EPR results (Fig. 5a). This meant that new OVs states

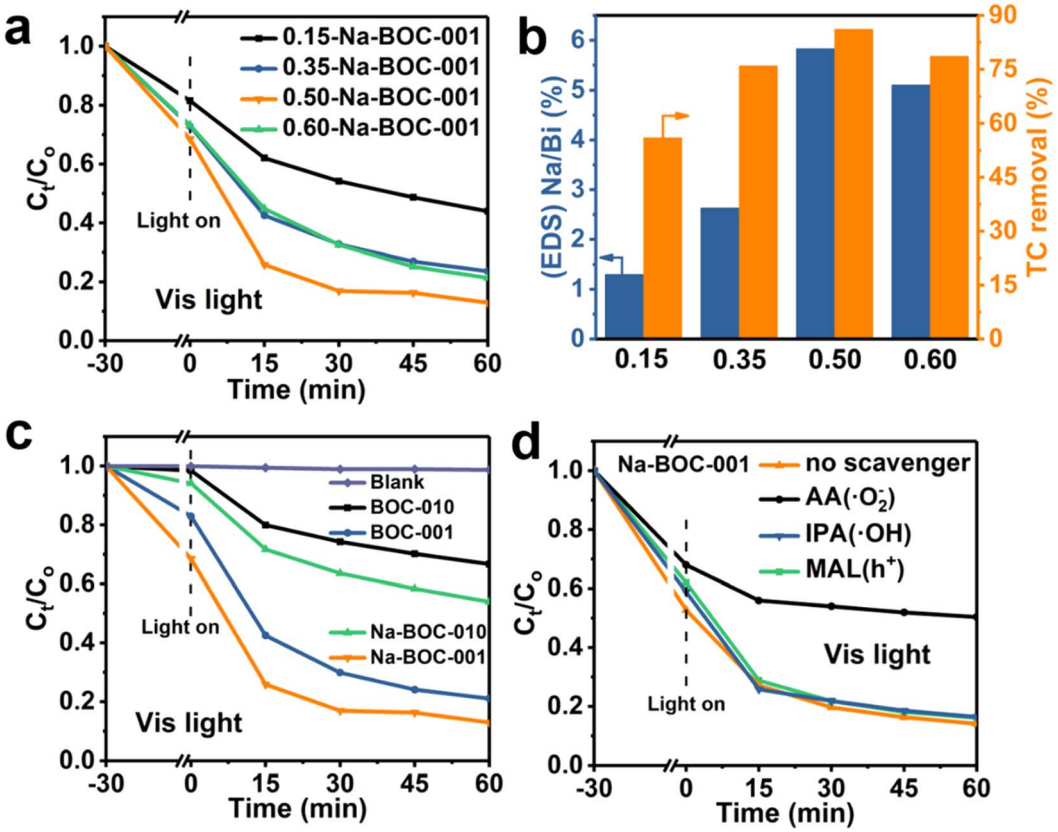

Fig. 9 (a) TC removal profiles *versus* time and (b) TC removal efficiency (maximum) and corresponding (EDS) Na/Bi ratio of *x*-Na-BOC-001 (*x* = 0.15, 0.35, 0.50 and 0.60) with different added [Na^+], (c) TC removal profiles *versus* time over no catalyst (blank), BOC-010, Na-BOC-010, BOC-001 and Na-BOC-001, (d) TC removal profiles *versus* time over Na-BOC-001 without and with addition of different scavengers. Conditions: [TC] = 20 mg L^{-1}; [catalyst] = 0.5 g L^{-1}; initial pH = 6.5, temperature = 25 °C; visible light (λ > 420 nm) irradiation.

were created between VB and CB of all samples under visible light irradiation, which acted as electron transition level so that the electrons in the VB of BOC samples could be excited to the OVs state by visible light and then continuously transferred to the CB.[49,54] Thus, photocatalytic degradation of all samples could be triggered by visible light irradiation, although the band gap values measured in the dark for all samples (3.40–3.48 eV) were relatively larger than the photon energy of visible light (<3.0 eV, that is >420 nm). Na-BOC-001 possessed the most newly formed OVs induced by the visible light, which was beneficial for promoting the electrons separation and transfer, leading to its strongest photocurrent among all samples, although its band gap measured in the dark were slightly wider than other counterparts. In addition, other reported the removal efficiency towards TC are displayed in Table S6.†[55–58]

In addition, to further investigate the effect of light wavelength on the photocatalytic performance, the TC removal efficiency and corresponding kinetic fitting results under other different wavelengths of light (UV-Vis and UV) irradiation were shown in Fig. S19a–d.† Meanwhile, the corresponding kinetic fitting results based in all the above figures were listed in Tables S3 and S4,† respectively. From the experimental results (Fig. S18, S19† and 9), it was clear that Na-BOC-001 exhibited the highest photocatalytic degradation efficiency and the fastest kinetic rate for target pollutant (TC) under either UV-Vis, UV or Vis light irradiation, among all the selected BOC samples. For Na-BOC-001, the maximum degradation efficiency obtained under both UV-Vis and UV irradiation were ~100%, which was much higher than that under Vis light irradiation (~87%). This indicated a significant effect of the wavelength on the photocatalytic performance in the order of UV-Vis > UV > Vis, which was in good agreement with the light absorption intensity in the UV-Vis DRS spectrum of Na-BOC-001 (Fig. 7a). In addition, the maximum degradation efficiency and kinetic rate of Na-BOC-001 under UV-Vis and UV light irradiation was only slightly higher than those of the other selected samples. Interestingly, the apparent rate constant (k) of the optimal Na-BOC-001 under Vis light irradiation was increased by a factor of 4.37 relative to the counterpart (BOC-010) without facet regulation and Na-doping, which was much higher than that of 1.69 under both UV-Vis and UV light irradiation. These results suggested that the synergistic effect of facet engineering and Na doping is more pronounced for Na-BOC-001 under the irradiation of Vis light than UV-Vis and UV light. Thus, the synergistic effect of facet engineering and Na doping on the photocatalytic performance and reaction mechanism under Vis light irradiation over all the selected BOC samples is the focus of investigation and discussion in this work.

To investigate the active species in the TC degradation process over Na-BOC-001, typical radical quenching tests were carried out with the addition of the corresponding radical scavengers, and the results are shown in Fig. 9d. Isopropanol (IPA, 10 mM), ascorbic acid (AA, 10 mM) and methanol (MAL, 10 mM) were served as the scavenger for the $^{\bullet}OH$, $^{\bullet}O_2^-$ and h^+ species, respectively.[53,59] As shown in Fig. 9d, a marginal difference is observed between the TC degradation curves in the presence of IPA, MAL and without addition of scavenger, indicating minor contribution of $^{\bullet}OH$ and h^+ in the photocatalysis of TC. However, a significant suppression in the removal efficiency of TC (decreased from 86.4 to 50.25%) is occurred after the addition of AA, demonstrating that the $^{\bullet}O_2^-$ radicals are the main active species. The main species in the TC degradation process over BOC-001 are the same as that of Na-BOC-001 (Fig. S20†), which reveals that the Na doping has a negligible effect on the main active species involved in the TC photocatalysis.

3.9. Photocatalysis mechanism

The identification of intermediate products is vital for revealing the detailed mechanism towards TC photocatalysis over Na-BOC-001. The intermediate products (P1–P18) were collected and detected by the HPLC-MS (Fig. S21–S30†). The results are identified according to the related literatures, and possible reaction pathways are proposed and shown in Fig. 10. There are two main pathways for the TC degradation under attack of free radicals ($^{\bullet}O_2^-$) from Na-BOC-001. In pathway I: TC is firstly converted into P1 through hydroxylation reaction.[60] Then, P2 is generated after the hydroxylation and deamidation of P1.[61] Furthermore, the P2 is transformed into four molecules (P3, P6,

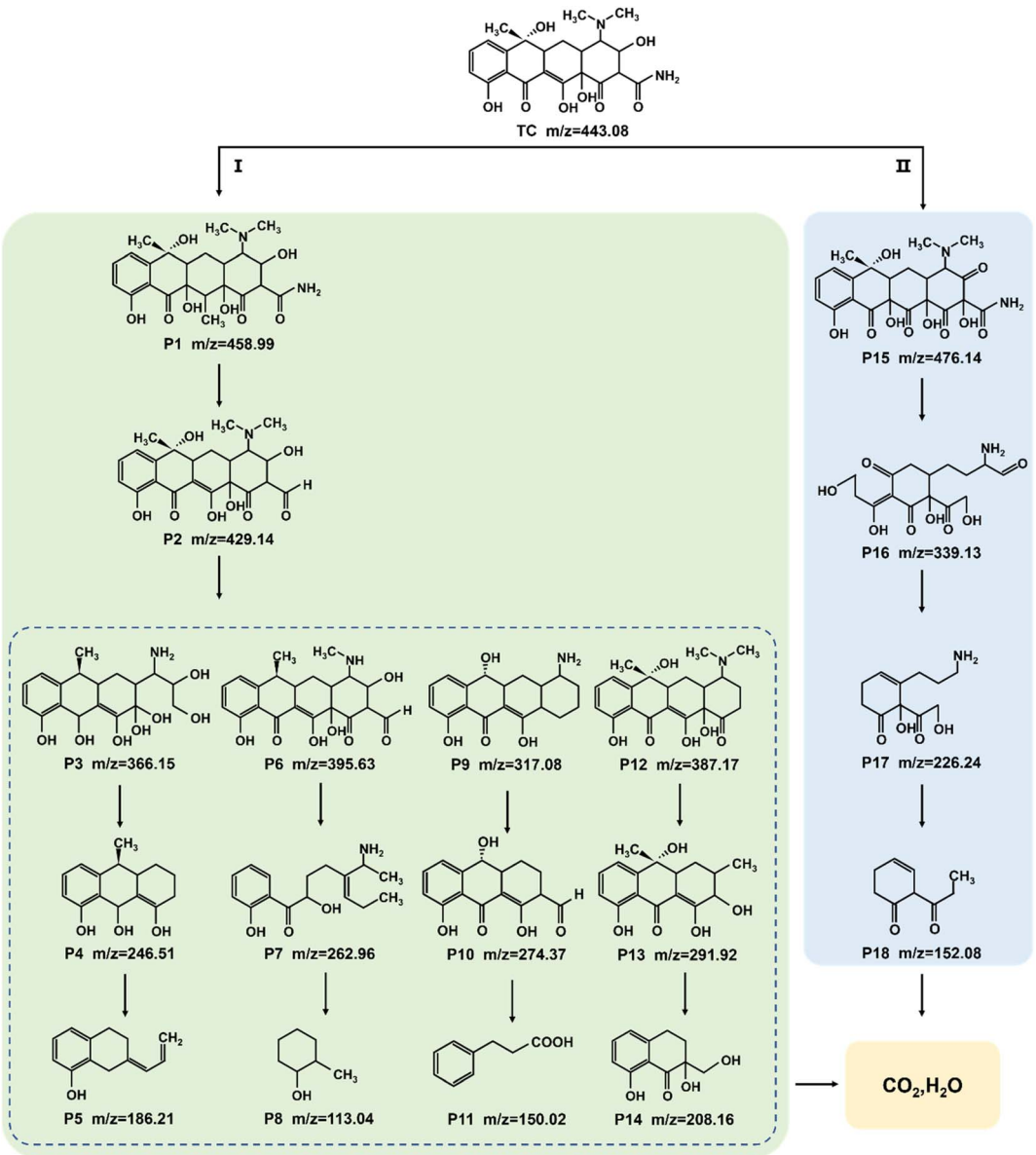

Fig. 10 Possible pathways for TC degradation over optimal Na-BOC-001 under visible light.

P9 and P12) whose conjugated structure is broken into P4, P7, P10 and P13, respectively. Sequentially, smaller molecules (P5, P8, P11 and P14) are separately obtained by the further ring opening of P4, P7, P10 and P13. In pathway II: P15 is converted *via* the double bond addition polymerization of TC, and then transformed into P16 by dehydroxylation, ring cracking and dealkylation.[61,62] The P16 is destructed into P17 and further to smaller P18. Finally, the partial smaller molecules presented in pathways I and II (P5, P8, P11, P14 and P18) can be degraded into CO_2 and H_2O, which has been confirmed by the TOC results (Fig. S31†).

Based on the above results, a possible photocatalytic mechanism for the photocatalysis of TC over the ultrathin Na-BOC-001 nanosheets under visible light irradiation is proposed (Fig. 11). Firstly, under visible light irradiation, electrons (e^-) in the VB could be excited to the OVs level of Na-BOC-001, and then continuously transferred to the CB, leading to the separation of e^- and holes (h^+) pairs, while the corresponding h^+ remained in the VB.[63,64] This charge transfer pathway could be verified mainly by the above EPR results that the visible light irradiation could cause the enhancement of OVs intensity than in the dark, which implied that new OVs sates have been generated between VB and CB in the band gap.[49] Additionally, the visible light enhanced OVs also indicated that there was more electrons trapped on the OVs,[54] which probably came from the excitation appeared on VB or CB. Combing with the above results (*I*–*t*, ESR and photocatalytic activity) can further indicated that photocatalytic reaction could be triggered (electrons could be excited) by visible light irradiation even if the values of bandgap of the sample were larger than the visible light. The electrons were excited by visible light and transferred from the VB to the CB of Na-BOC-001 only when the OVs acted as an electron transition level. Thus, the possible electron transfer pathway of Na-BOC-001 under visible light irradiation should be VB → OVs → CB. Similar pathway has also been reported in the previous literature.[49,54] Finally, the O_2 enriched on the surface was activated by the sufficient e^- for the generation of $^{\bullet}O_2^-$ radicals,[65] which will eventually attack the contaminant molecules (TC), leading to the decomposition of TC into CO_2 and H_2O.[66] The detailed reaction can be expressed follows:[52,53]

$$BiOCl + h\nu \rightarrow e^- + h^+ \quad (5)$$

$$e^- + O_2 \rightarrow {}^{\bullet}O_2^- \quad (6)$$

$$TC + {}^{\bullet}O_2^- \rightarrow CO_2 + H_2O \quad (7)$$

From the view of the photocatalytic reaction, conclusions can be drawn that the enhanced photocatalytic performance is greatly dependent on the optimized thermodynamics and kinetics of the dominant oxygen species ($^{\bullet}O_2^-$) generation (eqn (7)), which are closely related to the positive effects of Na-doped in the Na-BOC-001. From the thermodynamics aspect, more negative CB position in the band structure was achieved due to the Na doping effect, which provided stronger reduction potential for oxygen species ($^{\bullet}O_2^-$) generation than the non-doped BOC-001 (eqn (6)). For the kinetics, the resulted reduction of layer thickness and the role of interfacial electron transfer bridge are favorable for accelerating the photoinduced e^- and h^+ separation/transfer, leading to the increasing photoelectron amount and photocurrent (eqn (5) and (6)). Moreover, the Na-doped surface with more light-controlled OVs showed preferential adsorption for the O_2 molecules (eqn (6)), which is beneficial for quickly replenish the O_2 consumed over the BiOCl, thus sustainably promoting the O_2 activation.

3.10. Reusability

The chemical stability and repeatability are crucial for catalyst to application. Five cycles TC degradation experiments were

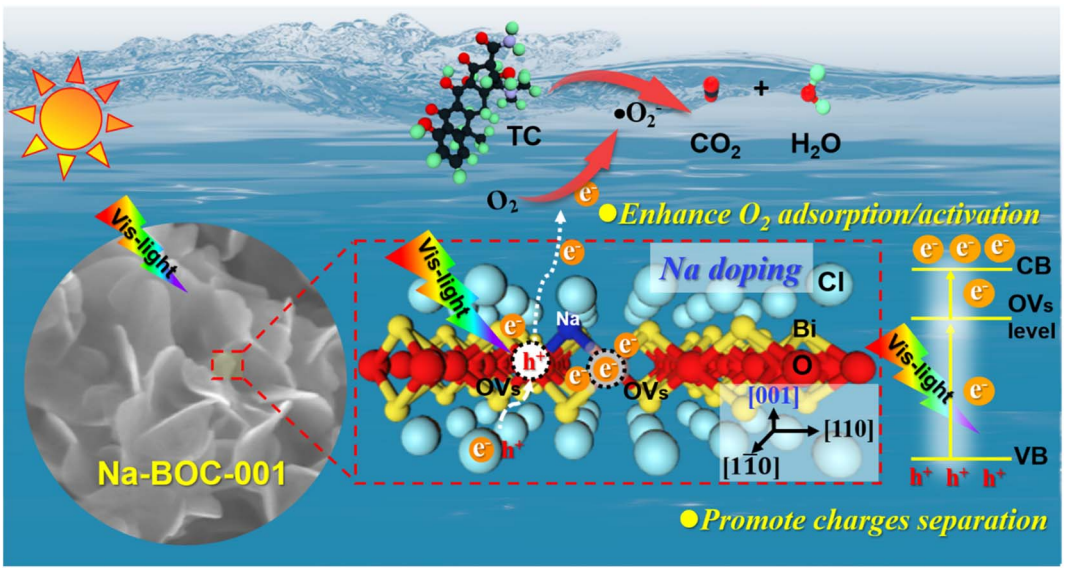

Fig. 11 Proposed mechanism for photocatalysis of TC over ultrathin Na-BOC-001 nanosheets under visible light irradiation.

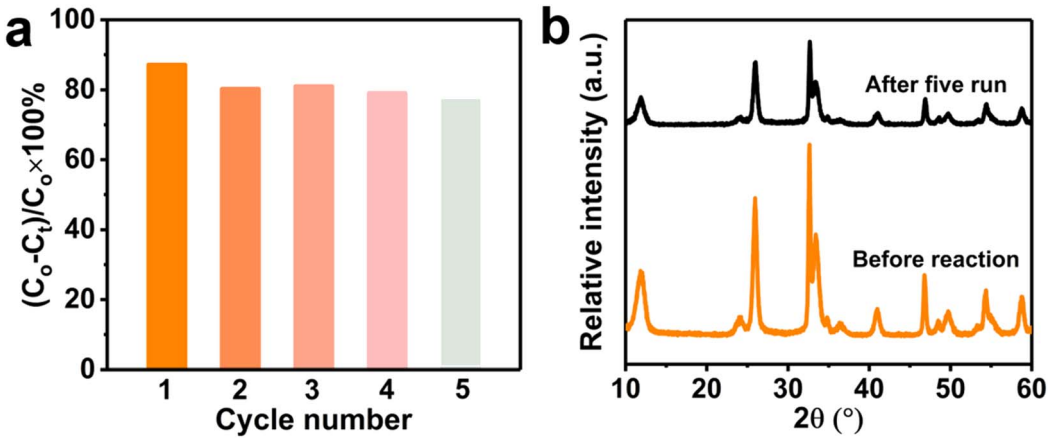

Fig. 12 Recycle experiments of Na-BOC-001 for (a) degrading TC and (b) XRD patterns before and after reaction. Conditions: [TC] = 20 mg L^{-1}, [catalyst] = 0.5 g L^{-1}, pH = 6.5, T = 25 °C, visible light (λ > 420 nm).

carried out to investigate the stability and reusability for the Na-BOC-001 (Fig. 12a). The catalyst was collected by filtering when accomplished the catalytic, then soaked in deionized water for 4 h. After that, cleaning the catalyst with deionized water and absolute ethanol, and finally dried under vacuum at 80 °C for 8 h. After five recycle runs, the Na-BOC-001 reduced the degradation efficiency for TC was only reduced by 10.1% under visible light irradiation, which indicate the Na-BOC-001 photocatalyst exhibit adequate photocatalytic degradation ability and recycling ability. In addition, the XRD patterns (Fig. 12b) shown there is no distinct change before and after cycling. The above results demonstrated that the Na-BOC-001 has acceptable chemical stability and repeatability.

4. Conclusions

In summary, a series of BiOCl based photocatalysts (BOCs) have been successfully synthesized *via* a facile one-step facet regulation and Na doping. Specially, the thickness of *x*-Na-BOC-001 (x = 0.15, 0.35, 0.50 and 0.60) has a good negative linear dependence on the effective doping ratio of Na ((EDS) Na/Bi). The ultrathin Na-BOC-001 nanosheets with highly exposed {001} facets and the severe lattice shrinkage have been obtained at the added [Na^+] of 0.50 mM, which possesses the smallest atomic layer thickness (<4 nm), the highest Na doping ratio ((EDS)Na/Bi: 5.83%), and the largest content of OVs owing to the synergistic effect of {001} facets and Na doping. In comparison to other bulk counterparts (Na-BOC-010, BOC-001 and BOC-010), the ultrathin Na-BOC-001 has surfaces with preferential adsorption for O_2, efficient separation of charges, and favorable CB position for O_2 activation, leading to the largest amount of ROS generated under visible light irradiation. As a result, the highest visible-light-driven removal efficiency (~87%) for TC have been achieved over the Na-BOC-001. This work may shed light on the synergistic effect of facet engineering and alkali metal doping, which paves a new way for the development of highly active semiconductors for visible-light-driven photocatalytic applications.

Author contributions

Kunyu Chen: investigation, data curation, formal analysis, writing – original draft. Yiwei Huang: investigation, data curation, validation. Meina Huang: funding acquisition, writing – review & editing. Yanqiu Zhu: resources, review & editing. Ming Tang: data curation. Renjie Bi: data curation. Meiping Zhu: conceptualization, supervision, funding acquisition, project administration, data analysis, visualization, writing – original draft, writing – review & editing.

Conflicts of interest

The authors declare that they have no known competing financial interests or personal relationships that could have appeared to influence the work reported in this paper.

Acknowledgements

This research was financially supported by Guangxi Natural Science Foundation (No. 2021GXNSFBA220074), Opening Project of Guangxi Key Laboratory of Petrochemical Resource Processing and Process Intensification Technology Scientific Research Foundation of Guangxi University (No. 2021K010) and Youth Cultivating Foundation of South China Normal University (No. 21KJ11).

References

1 Q. Zeng, J. Li, L. Li, J. Bai, L. Xia and B. Zhou, *Appl. Catal., B*, 2017, **217**, 21–29.
2 S. Reardon, *Nature*, 2014, **509**, 141–142.
3 H. Li, J. Shi, K. Zhao and L. Zhang, *Nanoscale*, 2014, **6**, 14168–14173.
4 H. Jung, R. Koutavarapu, S. Lee, J. Kim, H. Choi and M. Choi, *J. Alloys Compd.*, 2018, **735**, 2058–2066.
5 Z. Wu, Y. Xue, X. He, Y. Li, X. Yang, Z. Wu and G. Cravotto, *J. Hazard. Mater.*, 2020, **387**, 122019.

6 X. Hu, Y. Zhang, B. Wang, H. Li and W. Dong, *Appl. Catal., B*, 2019, **256**, 117789.
7 J. Li, S. Cai, Z. Xu, X. Chen, J. Chen, H. Jia and J. Chen, *J. Hazard. Mater.*, 2017, **325**, 261–270.
8 Y. Yang, C. Zhang, C. Lai, G. Zeng, D. Huang, M. Cheng, J. Wang, F. Chen, C. Zhou and W. Xiong, *Adv. Colloid Interface Sci.*, 2018, **254**, 76–93.
9 Z. Wang, Z. Chu, C. Dong, Z. Wang, S. Yao, H. Gao, Z. Liu, Y. Liu, B. Yang and H. Zhang, *ACS Appl. Nano Mater.*, 2020, **3**, 1981–1991.
10 H. Pan, L. Feng, W. Zeng, Q. Zhang, X. Zhang and Z. Liu, *Inorg. Chem.*, 2019, **58**, 13195–13202.
11 M. Shahid, R. Mehmood, M. Athar, J. Hussain, Y. Wei and A. Khaliq, *ACS Appl. Nano Mater.*, 2020, **4**, 746–758.
12 B. Li, L. Shao, R. Wang, X. Dong, F. Zhao, P. Gao and Z. Li, *J. Mater. Chem. A*, 2018, **6**, 6344–6355.
13 M. Shahid, Y. Wei, J. Wang, G. Chen, D. Gao, C. Ye, Y. Sun, G. Liu and C. Li, *ChemPlusChem*, 2019, **84**, 828–837.
14 J. Jiang, K. Zhao, X. Xiao and L. Zhang, *J. Am. Chem. Soc.*, 2012, **134**, 4473–4476.
15 K. Zhao, L. Zhang, J. Wang, Q. Li, W. He and J. Yin, *J. Am. Chem. Soc.*, 2013, **135**, 15750–15753.
16 Q. Zhou, W. Huang, C. Xu, X. Liu, K. Yang, D. Li, Y. Hou and D. Dionysiou, *Chem. Eng. J.*, 2021, **420**, 129582.
17 H. Li, J. Li, Z. Ai, F. Jia and L. Zhang, *Angew. Chem., Int. Ed.*, 2018, **57**, 122–138.
18 L. Yang, J. Guo, J. Zhang, S. Zhang, W. Dai, X. Xiao, X. Luo and S. Luo, *Chem. Eng. J.*, 2022, **427**, 131550.
19 Y. Tan, Q. Zhou, W. Huang, K. Lu, K. Yang, X. Chen, D. Li and D. Dionysiou, *Environ. Sci.: Nano*, 2023, **10**, 215–228.
20 F. Deng, Y. Luo, H. Li, B. Xia, X. Luo, S. Luo and D. Dionysiou, *J. Hazard. Mater.*, 2020, **383**, 121127.
21 S. Wu, H. Yu, S. Chen and X. Quan, *ACS Catal.*, 2020, **10**, 14380–14389.
22 W. Yan, L. Yan and C. Jing, *Appl. Catal., B*, 2019, **244**, 475–485.
23 D. Ma, L. Yang, Z. Sheng and Y. Chen, *Chem. Eng. J.*, 2021, **405**, 126538.
24 Y. Ren, J. Zou, K. Jing, Y. Liu, B. Guo, Y. Song, Y. Yu and L. Wu, *J. Catal.*, 2019, **380**, 123–131.
25 L. Ye, X. Jin, C. Liu, C. Ding, H. Xie, K. Chu and P. Wong, *Appl. Catal., B*, 2016, **187**, 281–290.
26 M. Guan, C. Xiao, J. Zhang, S. Fan, R. An, Q. Cheng, J. Xie, M. Zhou, B. Ye and Y. Xie, *J. Am. Chem. Soc.*, 2013, **135**, 10411–10417.
27 H. Ma, Y. He, P. Chen, H. Wang, Y. Sun, J. Li, F. Dong, G. Xie and J. Sheng, *Chem. Eng. J.*, 2021, **417**, 129305.
28 J. Xiong, P. Song, J. Di, H. Li and Z. Liu, *J. Mater. Chem. A*, 2019, **7**, 25203–25226.
29 P. Zhou, Y. Shen, S. Zhao, G. Li, B. Cui, D. Wei and Y. Shen, *Chem. Eng. J.*, 2021, **407**, 126697.
30 T. Shen, X. Shi, J. Guo, J. Li and S. Yuan, *Chem. Eng. J.*, 2021, **408**, 128014.
31 Y. Li, T. Wang, W. Ren, J. Han, Z. Yin, J. Qiu, Z. Yang and Z. Song, *ACS Appl. Nano Mater.*, 2019, **2**, 7652–7660.
32 W. Li, W. Huang, H. Zhou, H. Yin, Y. Zheng and X. Song, *J. Alloys Compd.*, 2015, **638**, 148–154.
33 Z. Zhu, I. Chu, Z. Deng and S. Ong, *Chem. Mater.*, 2015, **27**, 8318–8325.
34 X. Zhang, C. Fan, Y. Wang, Y. Wang, Z. Liang and P. Han, *Comput. Mater. Sci.*, 2013, **71**, 135–145.
35 W. Kim, D. Pradhan, B. Min and Y. Sohn, *Appl. Catal., B*, 2014, **147**, 711–725.
36 Y. Myung, J. Choi, F. Wu, S. Banerjee, E. Majzoub, J. Jin, S. Son, P. Braun and P. Banerjee, *ACS Appl. Mater. Interfaces*, 2017, **9**, 14187–14196.
37 S. Weng, Z. Pei, Z. Zheng, J. Hu and P. Liu, *ACS Appl. Mater. Interfaces*, 2013, **5**, 12380–12386.
38 S. Wu, X. Yu, J. Zhang, Y. Zhang, Y. Zhu and M. Zhu, *Chem. Eng. J.*, 2021, **411**, 128555.
39 Q. Wang, W. Wang, L. Zhong, D. Liu, X. Cao and F. Cui, *Appl. Catal., B*, 2018, **220**, 290–302.
40 T. Narenuch, T. Senasu, T. Chankhanittha and S. Nanan, *J. Solid State Chem.*, 2021, **294**, 121824.
41 X. Li, Z. Hu, Q. Li, M. Lei, J. Fan, S. Carabineiro, Y. Liu and K. Lv, *Chem. Commun.*, 2020, **56**, 14195–14198.
42 J. Cao, J. Li, W. Chu and W. Cen, *Chem. Eng. J.*, 2020, **400**, 125813.
43 X. Yuan, D. Shen, Q. Zhang, H. Zou, Z. Liu and F. Peng, *Chem. Eng. J.*, 2019, **369**, 292–301.
44 S. Wang, X. Hai, X. Ding, K. Chang, Y. Xiang, X. Meng, Z. Yang, H. Chen and J. Ye, *Adv. Mater.*, 2017, **29**, 1701774.
45 X. Chen, X. Chen, E. Yu, S. Cai, H. Jia, J. Chen and P. Liang, *Chem. Eng. J.*, 2018, **344**, 469–479.
46 J. Sun, X. Li, Q. Zhao and B. Liu, *Appl. Catal., B*, 2021, **281**, 119478.
47 X. Zhang, D. Li, G. Zhu, T. Lu and L. Pan, *J. Colloid Interface Sci.*, 2017, **499**, 145–150.
48 D. Xu, H. Feng, Y. Dong, Q. Wang, G. Zhang, L. Lv, Z. Ren and P. Wang, *Adv. Mater. Interfaces*, 2020, **7**, 2000548.
49 D. Cui, L. Wang, K. Xu, L. Ren, L. Wang, Y. Yu, Y. Du and W. Hao, *J. Mater. Chem. A*, 2018, **6**, 2193–2199.
50 C. Mao, H. Cheng, H. Tian, H. Li, W. Xiao, H. Xu, J. Zhao and L. Zhang, *Appl. Catal., B*, 2018, **228**, 87–96.
51 H. Huang, K. Xiao, N. Tian, F. Dong, T. Zhang, X. Du and Y. Zhang, *J. Mater. Chem. A*, 2017, **5**, 17452–17463.
52 R. Yang, Z. Zhu, C. Hu, S. Zhong, L. Zhang, B. Liu and W. Wang, *Chem. Eng. J.*, 2020, **390**, 124522.
53 Q. Wang, J. Huang, H. Sun, K. Zhang and Y. Lai, *Nanoscale*, 2017, **9**, 16046–16058.
54 I. Nakamura, N. Negishi, S. Kutsuna, T. Ihara, S. Sugihara and K. Takeuchi, *J. Mol. Catal. A: Chem.*, 2020, **161**, 205–212.
55 F. Zhang, X. Xiao and Y. Xiao, *Dalton Trans.*, 2022, **51**, 10992–11004.
56 F. Xu, Q. Zhang, R. An, L. Li and L. Zhou, *J. Alloys Compd.*, 2022, **899**, 163324.
57 J. Cao, W. Cen, Y. Jing, Z. Du, W. Chu and J. Li, *Chem. Eng. J.*, 2022, **435**, 134683.
58 Q. Hu, J. Di, B. Wang, M. Ji, Y. Chen, J. Xia, H. Li and Y. Zhao, *Appl. Surf. Sci.*, 2019, **466**, 525–534.
59 S. Dong, J. Hu, S. Xia, B. Wang, Z. Wang, T. Wang, W. Chen, Z. Ren, H. Fan, D. Dai, J. Cheng, X. Yang and C. Zhou, *ACS Catal.*, 2021, **11**, 2620–2630.

60 Z. Xie, Y. Feng, F. Wang, D. Chen, Q. Zhang, Y. Zeng, W. Lv and G. Liu, *Appl. Catal., B*, 2018, **229**, 96–104.
61 X. Huang, N. Zhu, X. Wei, Y. Ding, Y. Ke, P. Wu and Z. Liu, *J. Hazard. Mater.*, 2020, **400**, 123157.
62 Y. Zhang, J. Zhou, J. Chen, X. Feng and W. Cai, *J. Hazard. Mater.*, 2020, **392**, 122315.
63 W. Li, Z. Wang, Y. Li, J. Ghasemi, J. Li and G. Zhang, *J. Hazard. Mater.*, 2022, **424**, 127595.
64 X. Wang, Y. Ren, Y. Li and G. Zhang, *Chemosphere*, 2022, **287**, 132098.
65 Y. Wang, K. Wang, J. Wang, X. Wu and G. Zhang, *J. Mater. Sci. Technol.*, 2020, **56**, 236–243.
66 Z. Wang, Q. Cheng, X. Wang, J. Li, W. Li, Y. Li and G. Zhang, *Chem. Eng. J.*, 2021, **418**, 129460.